# DETERMINATION OF THE ORIENTATION OF OPEN FRACTURES FROM HYDROPHONE VSP

Jung Mo Lee and M. Nafi Toksöz

Earth Resources Laboratory
Department of Earth, Atmospheric, and Planetary Sciences
Massachusetts Institute of Technology
Cambridge, MA 02139

## ABSTRACT

Open fractures are of interest in many areas such as ground water contamination, hazardous waste disposal, oil and gas recovery, and geothermal energy extraction. In borehole geophysics and engineering, fractures are usually located by acoustic borehole televiewer logging, however, not all of the observed fractures are permeable. The caliper log, on the other hand, provides the information about the change of borehole diameter, but increasing diameter does not prove the existence of open fractures. Nor can the combination of these two methods—televiewer logs and caliper logs—provide direct information about open fractures. However, tube waves, generated by P- and/or S-waves in hydrophone vertical seismic profiling (VSP) or cross-well seismic profiling section can detect open fractures intersecting the borehole.

A new technique is developed to determine the orientation of open fractures using the normalized ratios of an S-wave-generated tube wave to a P-wave-generated tube wave. The fracture orientations determined by this method represent the average over the fracture planes for large radii, generally on the order of a meter. Numerical tests show that, given a good experiment design, a set of two independent measurements of these ratios with polarization information, or a set of three independent measurements without polarization information, provides a unique solution. The developed technique is stable in the presence of noise.

This technique is applied to hydrophone VSP data from the Kent Cliffs test well in southeastern New York state. The orientations of the three major fractures which generate primary tube waves in the seismic profiling sections are obtained. The results agree well with the orientations measured from the borehole televiewer images in general. Any discrepancy may be attributed to the difference between the sampling size of this method and the borehole televiewer, to the deviation of rays from the straight lines

due to inhomogeneity, and/or to possible SH-wave motion due to anisotropy and lateral inhomogeneity.

## INTRODUCTION

Permeable fractures which act as conduits for underground fluid play an important role in many areas, such as ground water contamination, hazardous waste disposal, oil and gas recovery, and geothermal energy extraction. In borehole geophysics and engineering, fractures are usually located by acoustic borehole televiewer logging. Not all of the observed fractures, however, are permeable. Improved methods for the discrimination and characterization of permeable fractures are of interest.

Hydrophone VSP's have been shown to detect open fractures (Huang and Hunter, 1981, 1982). The pressure disturbances inside a fluid-filled borehole caused by P- and S-waves were studied by White (1953), Schoenberg (1986), and Peng *et al.* (1994). Tube wave generation by a plane P-wave impinging on a fluid-filled borehole at intersections with open fractures was first modeled by Beydoun *et al.* (1985). This model was used by Hardin and Toksöz (1985), Hardin *et al.* (1987), and Toksöz *et al.* (1987, 1992) to characterize fractures from tube wave signals. Hardin and Toksöz (1985) and Hardin *et al.* (1987) used only P-waves and the tube waves generated by them. Toksöz *et al.* (1987) and Toksöz *et al.* (1992) attempted to determine the fracture dip by using the ratio of normalized tube waves generated by P- and SV-waves.

This study extends the model of Beydoun *et al.* (1985) to the case for impinging SV-waves, and the study of Toksöz *et al.* (1992) to utilize tube waves generated by both P- and SV-waves in determining the dip direction and dip angle of the intersecting fracture. The amplitude ratio of the tube wave generated by the impinging P-wave to the tube wave generated by the impinging SV-wave, after normalizing by the hydrophone response of the generating P- and SV-waves, respectively, is derived as a function of the fracture orientation. This forward modeling function is applied to invert for fracture orientation. After some numerical tests, the theoretical results are applied to the tube waves observed in hydrophone VSP sections collected at the Kent Cliffs test well in southeastern New York state.

## FORMALISM

In the model of Beydoun *et al.* (1985), fractures are idealized as parallel-plane, fluid-saturated, and embedded in an isotropic elastic medium. The authors treated the problem of a plane P-wave whose wave vector is in the plane of the fracture normal vector and the borehole axis vector. When a seismic wave impinges on a fracture, the fracture wall motion can be decomposed into two components: normal and parallel to the fracture plane. Beydoun *et al.* (1985) considered only the normal-plane motion. The fluid flow in a fracture due to parallel-plane motion was studied by Toksöz *et al.* (1992) with the same idealized model. It was shown that the volume of fluid flow due to

parallel-plane motion is several orders of magnitude less than that due to normal-plane motion. In this paper, we extend the model of Beydoun *et al.* (1985) for an impinging SV-wave. The geometry of the model will be generalized for the cases where the wave vector is not necessarily in the plane of the fracture normal vector and the borehole axis vector. The fluid flow, caused by the parallel motion, is treated as negligible.

In general, a plane SV-wave particle motion with a unit wave vector, $\hat{\mathbf{k}}$, can be described by

$$\mathbf{U}_{SV} = \frac{\hat{\mathbf{k}} \times (\hat{\mathbf{k}} \times \hat{\mathbf{z}})}{|\hat{\mathbf{k}} \times \hat{\mathbf{z}}|} U_{SV}, \tag{1}$$

where $\hat{\mathbf{z}}$ is the vertical unit vector. When this wave strikes a fracture with unit normal vector, $\hat{\mathbf{n}}$, the motion, $L(t)$, of the fracture wall in the normal ($\hat{\mathbf{n}}$) direction, driven by the SV-wave motion, with the assumption of very small strain, is given by

$$\begin{aligned} L(t) &= L_o - U_{SV}[\cos\phi \sin\psi \cos(S - A) - \sin\phi \cos\psi] \cos(\omega t) \\ &= L_o - \xi_{SV} \cos(\omega t). \end{aligned} \tag{2}$$

$A$ and $\phi$ are the azimuth and inclination (relative to the positive z-axis) of the wave vector, $S$ and $\psi$ are the dip direction (defined by up-dip azimuth) and dip angle of the fracture plane. $L_o$ is the static fracture width, and $\omega$ is the angular frequency of the impinging wave. The geometry is shown in Figure 1. We follow the derivation of Beydoun *et al.* (1985) with the following assumptions:

1. The fracture closure $\xi_{SV}$ is much smaller than the fracture width $L_o$; that is, the flow regime in the fracture is a linear, one-dimensional laminar flow such that Stokes' law is satisfied.

2. The fluid compressibility is small.

3. Fluid injected into the borehole does not significantly perturb the borehole pressure at the fracture location, and the pressure in the fracture is initially the same as in the borehole.

4. The wavelength of the incident waves is large compared to the fracture width and the borehole radius.

5. The intrinsic fracture permeability, $K$, is constant.

With these assumptions the time harmonic pressure disturbance, $P_{SV}^T$, in a borehole due to the fracture normal motion driven by a plane SV-wave is,

$$P_{SV}^T = \rho_f \omega^2 \xi_{SV} \chi(K) \left(\frac{K}{\pi\gamma\mu}\right)^{1/2} F(\omega, \xi_{SV}/L_o) \frac{(1 - c^2/\alpha_f^2)^{1/2}}{2(2 - c^2/\alpha_f^2) I_1(nR)} I_o(nr), \tag{3}$$

where,

$$\chi(K) = \frac{\sqrt{2KT/(\mu\gamma)}}{R \ln\{[\, R + \sqrt{2KT/(\mu\gamma)}\,]/R\}},$$

$$F(\omega, \xi_{SV}/L_o) = \omega \int_0^{T/2} \int_0^t \frac{1-(\xi_{SV}/L_o)\cos(\omega t)}{1-(\xi_{SV}/L_o)\cos(\omega\tau)} \frac{\sin(\omega\tau)}{(t-\tau)^{1/2}} d\tau dt,$$

and its asymptote for $\xi_{SV} \ll L_o$ (assumption 1) is

$$F(\omega, 0) = 2\omega \int_0^{T/2} (T/2 - t)^{1/2} \sin(\omega t)\, dt,$$

where $K$ fracture permeability,
$R$ borehole radius,
$T$ P-wave or tube wave period ($= 2\pi/\omega$),
$c$ tube wave phase velocity,
$n$ tube wave radial wavenumber from P-wave in fluid [$= k(1 - c^2/\alpha_f^2)^{1/2}$],
$r$ ellipsoidal fracture radius,
$\alpha_f$ P-wave (compressional wave) velocity of the fluid,
$\gamma$ fluid compressibility,
$\mu$ dynamic fluid viscosity, and
$\rho_f$ fluid density.

The amplitude of the normal motion of the fracture wall driven by a plane P-wave is

$$\xi_P = U_P[\sin\phi \sin\psi \cos(S - A) + \cos\phi \cos\psi]. \tag{4}$$

By exchanging this for $\xi_{SV}$ in equation (2) and following the same derivation to equation (3), we get the pressure disturbance in the intersecting borehole due to an impinging plane P-wave. If we compute the ratio of the normalized amplitudes, all the complicated fracture parameters except dip direction and angle are canceled out, and

$$\frac{P_{SV}^T/U_{SV}}{P_P^T/U_P} = \frac{\cos\phi \sin\psi \cos(S - A) - \sin\phi \cos\psi}{\sin\phi \sin\psi \cos(S - A) + \cos\phi \cos\psi}. \tag{5}$$

In general this is not a linear equation. However, the exact solution for the dip direction, $S$, and the dip angle, $\psi$, of the fracture can be obtained if two of these ratios from different wave vectors (different $A$ and $\phi$) are known and are independent. Special cases for equation (5) are where $\cos(S - A) = 1$. For these cases, the ray azimuth and the fracture dip direction are the same, and equation (5) becomes

$$\frac{P_{SV}^T/U_{SV}}{P_P^T/U_P} = \tan(\psi - \phi).$$

Furthermore, for the vertical incidence ($\phi = 0$) case, this simplifies to

$$\frac{P_{SV}^T/U_{SV}}{P_P^T/U_P} = \tan\psi.$$

These two equations were first introduced by Toksöz *et al.* (1992). Based on these special cases, equation (5) has been frequently interpreted by intuition as the apparent dip angle. It should be emphasized that in general equation (5) is not related to the apparent dip angle of the fracture. Note also that the apparent dip angle is given by the equation, $\tan^{-1}\{\tan\psi\cos(S-A)\}$.

The denominator and numerator of equation (5) are not dimensionless. In a real situation, the simultaneous measurement of tube wave pressures and P- and SV-wave displacements is difficult. Alternatively, we can relate the P- and SV-wave displacements to the pressures observed inside the borehole induced by these wave fields. At low frequencies (satisfied by assumption (4)) with a vertical borehole, the pressure field inside the borehole induced by an impinging plane P-wave with the amplitude $U_P$ is,

$$P_P = \frac{-i\omega\rho_f c^2\alpha}{\beta^2}\,\frac{1-2(\beta/\alpha)^2\cos^2\phi}{1-(c/\alpha)^2\cos^2\phi}\,U_P, \tag{6}$$

and by a SV-wave with the amplitude $U_{SV}$,

$$P_{SV} = \frac{-i\omega\rho_f c^2}{\beta}\,\frac{2\cos\phi\sin\phi}{1-(c/\beta)^2\cos^2\phi}\,U_{SV}, \tag{7}$$

where $\alpha$ is the P-wave velocity of the formation, and $\beta$ is the S-wave velocity of the formation. These equations were introduced by White (1953) and confirmed by Schoenberg (1986). They were used by Lee (1990) and more extensively by Peng *et al.* (1994) in hydrophone VSP modeling.

By combining equations (5), (6), and (7), we write

$$\Psi(S,\psi;A,\phi) = \frac{P_{SV}^T/P_{SV}}{P_P^T/P_P} = D\,\frac{\cos\phi\sin\psi\cos(S-A)-\sin\phi\cos\psi}{\sin\phi\sin\psi\cos(S-A)+\cos\phi\cos\psi}, \tag{8}$$

where

$$D = \frac{\alpha}{\beta}\,\frac{1-2(\beta/\alpha)^2\cos^2\phi}{1-(c/\alpha)^2\cos^2\phi}\,\frac{1-(c/\beta)^2\cos^2\phi}{2\cos\phi\sin\phi}.$$

The tube wave phase velocity for the case of open boreholes is, $c=[\rho_f(\frac{1}{\rho_f\alpha_f^2}+\frac{1}{\rho\beta^2})]^{-1/2}$, where $\rho$ is the formation density. The domain of $\Psi(S,\psi;A,\phi)$ is chosen as

$$\{(S,\psi,A,\phi)|\ 0\le S<2\pi,\ 0\le\psi\le\pi/2,\ 0\le A<2\pi,\ 0\le\phi\le\pi\},$$

in this study. It is clear that the range is $(-\infty,\ \infty)$.

The roots of $\Psi$ are located at (1) $\cos\phi=\pm\frac{\alpha}{\sqrt{2}\beta}$, (2) $\cos\phi=\pm\frac{\beta}{c}$, and (3) $\cot\psi=\cot\phi\cos(S-A)$. The first root would imply a very unrealistic case since usually $\frac{\alpha}{\sqrt{2}\beta}\ge 1$ and the equal sign appears only if the Poisson's ration is zero, which is not observed in naturally occurring earth materials. The second root is actually the pole of equation (7) and possibly occurs when the tube velocity is larger than the formation S-wave velocity. This is a well-known strong fluid resonance in soft formations. The third type roots

originate due to equation (5), and constitute lines in the $S\psi$-phase plane for a given set of $A$ and $\phi$.

The poles of $\Psi$ are located at (1) $\cos\phi{=}\pm\frac{\alpha}{c}$; (2) $\cos\phi{=}0$, $\sin\phi{=}0$; and (3) $\cot\psi{=}-\tan\phi\cos(S-A)$. The first pole, which is also the pole of equation (6) appears rarely in extremely soft formations and would generate a strong fluid resonance. The two poles of the second type appear at $\phi = \pm\pi/2$ and 0. These are the roots of equation (7) and imply no pressure disturbance from vertically or horizontally impinging SV-waves. The third type of poles originate from equation (5), and constitute lines in the $S\psi$-phase plane like the third type of roots. The first two types of poles depend on the inclination of the wave vector ($\phi$) and the material properties, and can be avoided by modifying the experiment design (changing $\phi$). On the other hand, the lines of the third type of poles are unavoidable.

Some special cases of equation (8) occur for dip, strike, and vertical incidences. For dip incidences ($S = A$ or $S = A + \pi$), the fracture dip angle can be immediately obtained as $\psi = \pm\tan^{-1}(D^{-1}\Psi)\pm\phi$. For the vertically or horizontally impinging waves, however, $P_{SV}$ is zero, as discussed previously, and $\Psi$ is at the second type pole. At some offset from these angles the pole is avoided. Another special case is the strike incidence ($A = S \pm \pi/2$). In this case equation (5) is reduced to $\Psi = D\tan\phi$, and all variables related to the fracture disappear. The same phenomenon occurs when the fractures are horizontal ($\psi = 0$), which is clear since no strike can be considered for horizontal fractures.

## NUMERICAL EXAMPLES AND INVERSION

In order to derive an appreciation for the formula and to establish a good inversion scheme, we have created some realistic forward models. Values of $\Psi$ as a function of $S$ and $\psi$ for hard and soft formations are considered. The hard formation is assumed to be the Solenhofen limestone whose P- and S-wave velocities are 5970 and 2880 m/s and density is 2656 kg/m$^3$. Using the compressional wave velocity of 1484 m/s and 1000 kg/m$^3$ for the density of the borehole fluid, the tube wave velocity for this hard formation is 1430 m/s. The soft formation is assumed to be the Pierre shale whose P- and S-wave velocities are 2074 and 869 m/s with density of 2000 kg/m$^3$. The resulting tube wave velocity for this soft formation is 950 m/s using the same borehole fluid parameters. For each formation, three VSP cases are considered: near, intermediate, and far offset, using $15^o$, $45^o$, and $75^o$ for the wave vector inclination, $\phi$. The wave vector azimuth is fixed at zero (plane waves incoming from the north).

For all six cases, forward computations of $\Psi(S,\psi)$ are carried out for every integer angle of $S$ and $\psi$ in degrees, and the results are shown in Figure 2. To help visualization, the dynamic range of the color scale is established individually in each case. The dimensionless ranges are, from $-20$ to 20, from $-10$ to 10, and from $-7$ to 7 for near, intermediate, and far offset in the hard formation, respectively. In the soft formation, the ranges are from $-10$ to 10, from $-7$ to 7, and from $-3$ to 3 for near, intermediate,

and far offset. The fluid resonance incident angle, where $\cos\phi = \pm\frac{\beta}{c}$, for soft formations ($\pm 23.83^o$ for these examples) are avoided by the choice of incident angles.

Figure 2 shows some of the distinctive behavior of function $\Psi$. First of all, the lines of poles due to the equation, $\cot\psi = -\tan\phi\cos(S-A)$, occur on the boundary line of minimum and maximum values (purple and red) in the figure. The strike incidences and the horizontal fractures appear as predicted. The strike incidences appear when dip direction is 90 or $270^o$ in these examples, and $\Psi$ does not depend on the dip angle. For the horizontal fracture, $\Psi$ is independent of the dip direction. An important influence on the value of $\Psi$ is the weighting factor of coefficient $D$. This can be controlled by experiment design. For a given formation (fixed seismic velocities and density), the experimental geometry should be chosen (with choice of $\phi$) to make $D$ value reasonably large and consequently make $\Psi$, sensitive to the fracture parameters. A single datum determines a curve in the $S\psi$-plane, corresponding $\Psi$ equals to a constant. With two independent data, two such curves can be found and the intersecting point of these indicates fracture dip angle and direction. However, when the waves with the same azimuth or the opposite azimuth with different inclination are used, the curves are congruent with each other. Furthermore, the only possible solutions are $S = A \pm 90^o$ and $\psi = 90^o$ for this geometry if measurement errors are included. These should be considered carefully if the data are collected to invert for the fracture parameters.

The inverse problem is more difficult than the forward problem. The difficulties come from the unavoidable lines of poles defined by the equation, $\cot\psi = -\tan\phi\cos(S-A)$, and from observational noise. In reality, the measured quantities in seismic sections are $P_P$, $P_{SV}$, $P_P^T$, and $P_{SV}^T$. When $P_P$ and/or $P_{SV}$ are small, the values $P_P^T/P_P$ and/or $P_{SV}^T/P_{SV}$ become large and are seriously corrupted by the noise of $P_P$ and/or $P_{SV}$. In order to overcome this problem, we define a new function, $\Theta$, as

$$\Theta(S,\psi;A,\phi) = \tan^{-1}\Psi = \tan^{-1}[D\,\frac{\cos\phi\sin\psi\cos(S-A) - \sin\phi\cos\psi}{\sin\phi\sin\psi\cos(S-A) + \cos\phi\cos\psi}]. \tag{9}$$

This function segregates the individual noises in the following manner. When $P_{SV}$ is small, $\Theta$ depends mainly on the value of $P_P^T/P_P$. On the other hand, $\Theta$ mostly depends on the value of $P_{SV}^T/P_{SV}$ when $P_P$ is small. Note that this transform changes the pole lines in $\Psi$ into jump discontinuities in $\Theta$ by $\pm\pi$.

Based on the least-square approach, the individual misfit, $\varepsilon$, is defined by

$$\varepsilon(S,\psi;A_k,\phi_k) = \left[\Theta(A_k,\phi_k)^{\text{obs}} - \Theta(S,\psi;\ A_k,\phi_k)^{\text{calc}}\right]^2.$$

The subscript $k$ is introduced here to signify the discrete observations of $\Theta$. The solution for the inversion is the set of model parameters $(S,\psi)$ that gives the smallest total misfit function of all observations:

$$\varepsilon(S,\psi) = \sum_{k=1}^{N}\varepsilon(S,\psi;A_k,\phi_k) = \min, \tag{10}$$

where $N$ is the number of the observations.

Shown here is a two-dimensional inversion of the dip direction and dip angle of a fracture. However, the model function, $\Theta$, is not well-behaved. It is difficult to develop an inversion algorithm to overcome this ill-posedness. With observational noise, no more than one degree resolution is expected in inversion. In this case only $360 \times 91$ discrete values of the misfit function need to be computed for each observation. These are very affordable quantities for computations with current computer speeds. What remains is the summing of the misfit functions from all observations and finding the minimum. It is important to note that it is not easy to keep track of the polarization information. Although the final equation does not include any factor that might distort the waveforms, the different order of angular frequency, $\omega$, terms in equations (3) and (6) implies a different order time derivative of the time signal. Inversions without polarization information, using the absolute value of equation (8), are also attempted.

A series of synthetic data are inverted to test the performance and stability of the inversion. A multi-offset VSP geometry is employed for these tests. A fracture is assumed to be located at a 300m depth with $180^o$ dip direction and $45^o$ dip angle. Four shot points are chosen as 200 m offset with $300^o$ azimuth, 500 m offset with $210^o$ azimuth, 400 m offset with $110^o$ azimuth, and 600 m offset with $330^o$ azimuth. They are named S/P 1, S/P 2, S/P3, and S/P 4, respectively. The schematic diagram of the experimental geometry is shown in Figure 3. The input data of the normalized tube wave amplitude ratios for each shot point are synthesized using equation (8) with an assumed homogeneous hard formation with Vp=5970 m/s, Vs=2880 m/s, and $\rho$=2656 kg/m$^3$.

The results are shown in Figure 4. These figures are color maps of the total misfit functions defined by equation (10). The vertical axes represent the fracture dip angles and the horizontal axes represent the dip directions in degrees. To help visualization, the misfit values of less than 0.002 are represented in black, where the global minima reside. One can consider the black-colored area to be a confidence region on the parameters–dip direction and angle, however the confidence level of the region is not known. Only misfit values for the range from $90^o$ to $270^o$ of the fracture dip direction are presented since the remaining range is meaningless.

Figures 4A and B use data from VSP geometry with two shot points of 200 m offset with $300^o$ azimuth and 500 m offset with $210^o$ azimuth (S/P 1 and S/P 2). Figures 4C and D use data from VSP geometry with three shot points of 200 m offset with $300^o$ azimuth, 500 m offset with $210^o$ azimuth, and 400 m offset with $110^o$ (S/P 1, S/P 2, and S/P 3). Figures 4E,F,G,H,I, and J use data from VSP geometry with three shot points of 500 m offset with $210^o$ azimuth, 400 m offset with $110^o$ azimuth, and 600 m offset with $330^o$ azimuth (S/P 2, S/P 3, and S/P 4). Figures 4A, C, and E use polarization information, and the others use only the absolute ratio values. Noise is introduced by perturbing the amplitude ratios. Tube wave amplitude ratios for all three shot points are increased by 5% and 10% for Figures 4G and I, respectively. Tube wave amplitude ratios for all three shot points are decreased by 5% and 10% for Figures 4H and J, respectively.

### Fracture Orientation From Hydrophone VSP

It is shown in Figure 4A that the solution can be found uniquely when a perfect set of two independent data are supplied. The solution is not unique in Figure 4B because the polarization information is not used, i.e., for any observations, two models producing opposite polarizations yields the same misfit. One more shot point is added for Figures 4C and D with azimuth almost opposite to one of the initial shot points ($10^o$ deviated). Although no significant improvement can be seen in Figure 4C, the solution becomes unique in Figure 4D. The misfit function for the nearest shot point is much more sensitive than it is for others. This is reflected in Figures 4A–D, the black colored strip represents portions of curves from the individual misfit values of the nearest shot point. Shot points are arranged in a better manner—better azimuthal distribution and less inclination variation for the wave vectors. The distributions of the misfit values appear much better in Figures 4E and F. In Figures 4A, C, D, E, and F, the global minimum always points to the input model since noise has not been included. Figures 4G–J show the stability of the misfit function with respect to the existence of noise. Five percent noise modifies the position of the global minimum by one degree in both dip direction and dip angle. Ten percent noise causes a deviation of two degrees.

## KENT CLIFFS EXPERIMENT

### Kent Cliffs Borehole

The Kent Cliffs borehole is an approximately 1-km-deep borehole located in southeastern New York state. Its coordinates are $41^o27'01''$ and $73^o44'45''$W. It is a purely scientific test well for the study of the crustal stress regime and for the appraisal of seismic hazard in the surrounding region. Geologically, the borehole is located in the northern Reading prong (locally called the Hudson highlands) which is composed of Precambrian crystalline rocks. It is close to the north end of the surface trace of the Ramapo-Canopus fault system whose major axis strikes northeasterly (Ratcliffe, 1971). The borehole cuts first through amphibolite then through underlying gneiss. The contact between these two formations which strikes N60°E and dips 65°SE intersects the borehole at a depth of 271 m. Both formations show a well-developed foliation sub-parallel to the contact (Statton, 1986). The site is characterized by a number of geophysical experiments including well-logs, hydraulic fracturing stress measurements, core sample ultrasonic velocity measurements, three-component VSP, and hydrophone VSP (see Lee, 1990, for details). In this section, we apply our method to determine the orientation of the open fractures from primary tube waves observed in hydrophone VSP sections.

### Hydrophone VSP

The multiple offset hydrophone VSP experiment was carried out using a repeatable vertical impact source. The source was an accelerated weight drop source. The downhole sensors employed were a group of six linked downhole piezo-electric hydrophones sepa-

rated by a 3.048 m interval for a total group length of 15.24 m. When the hydrophone group was moved by 15.24 m, the position of the last hydrophone in the previous group became the position of the first hydrophone of the new group such that every fifth location was observed twice as often as other locations. This downhole hydrophone arrangement provided a measurement of the observational error by comparing the data at the overlapping, repeated depths. The source impacts were repeated four to six times for each hydrophone group. The source offsets were 37.5, 350.5, and 288.0 m, with azimuths of $268^o$, $318^o$, and $85^o$, respectively, as shown in Figure 5. The source elevations relative to the well head are 0.0, $-3.4$, and $-12.2$ m, respectively. The source location will be called S/P#1, S/P#2, and S/P#3, respectively. Two seconds recordings were made with a sampling rate of 0.5 ms. In addition to the source base plate geophone that records accurate source time breaks, a source monitor geophone was set up about 5 m.

## Data Processing

In order to increase the signal-to-noise ratio, the raw data edited and stacked. The amplitude of each stacked trace is normalized utilizing the amplitude of the corresponding source monitor phone record. A phaseless Butterworth band-pass filter of 80 Hz $-6$ dB low cut-off and 200 Hz $-6$ dB high cut-off was applied to the stacked data. The processed sections are shown in Figures 6, 7, and 8. These VSP sections show tube wave trains of large amplitude (the chevron-shaped signals), and P- and S-wave trains of small amplitude. The primary tube waves are generated at depths of about 232, 287, and 513 m.

## Relevant Geophysical Experiments

Among the geophysical experiments carried out at the Kent Cliffs test site, borehole televiewer logging and caliper loggings were used to identify fractures intersecting the borehole. The borehole televiewer images around these depths are shown in Figure 9. From these televiewer images, the dip direction and angle of the fractures are measured and presented in Table 1. It is worthwhile to note the following: (1) these measurements reflect only the orientation of the fracture at the cross-sectional area intersected by the borehole; (2) the dip angle may be exaggerated because the part of the fracture which intersects the borehole by an acute angle can be easily chipped away; and (3) the measurement error can easily become more than $10^o$ in both dip direction and angle based on scale and quality of the image. In addition to the major open fractures that generate major tube waves, borehole televiewer logging shows extensive small scale, closed fracturing throughout the entire depth of the well. The fracture density (number of fractures per 10 m), as a function of the depth, obtained from the televiewer logging is shown in Figure 10A. As seen in this figure, it is difficult to correlate the locations of the major open fractures with the fracture density. These major open fractures can be identified in the caliper log. The caliper log sections at the depths around these

fractures are shown in Figure 10B. It should be emphasized that neither one nor a combination of the two logs can identify the major open fractures without the aid of hydrophone VSP sections.

## Analysis of Hydrophone VSP

In order to use the previously developed technique in determining the orientation of open fractures, the amplitude ratios must be measured in the hydrophone VSP sections. It is required that the tube wave fields and the P- and S-wave fields be separately isolated from the total observed wave fields. Wave field isolation is carried out by applying a fan-shaped $f$-$k$ filter with cut-off velocity at 2.54 km/s, since the observed P-, S-, and tube wave velocities are approximately 7.0, 3.5, and 1.5 km/s, respectively (see Lee and Alexander, 1989, for details in filter design). The resulting filtered sections are shown in Figures 11 through 16. Figures 11, 12, and 13 show the $f$-$k$ filtered sections which retain the P- and S-waves and reject the tube waves. The P- and S-waves are significantly enhanced in each record section as the much larger tube waves are effectively eliminated. Figures 14, 15, and 16 show the $f$-$k$ filtered sections which retain the tube waves and reject the P- and S-waves. Strong up- and down-going tube waves are being generated at several depths as seen in Figures 6 through 8 where tube wave onsets coincide with arrival times of P- and S-waves.

The wave field isolation is expected to provide a relatively accurate estimate of the amplitudes of P-, S-, and tube waves. Detailed observation of $f$-$k$ filtered sections, however, show that P- and S-waves at the onsets of tube waves (at the fractures) are still corrupted. As are the tube waves. This problem has been overcome by selecting and stacking neighboring traces. In order to remove geometric spreading and attenuation effects for P- and S-waves, traces are chosen symmetrically around the fracture depths (usually six to eight traces), and shifted by appropriate velocities and stacked. This procedure is similar to waveform interpolation. The stacking also improves the signal-to-noise ratio. Tube wave traces are also stacked to improve the signal-to-noise ratio. Since tube waves do not undergo geometrical spreading, traces are chosen without consideration of the symmetry. The normalized amplitude ratios have been estimated by two independent methods—the ratio of rms amplitudes and the average of spectral ratio. The rms amplitude ratio method consists of the following: (1) the tube waves and the corresponding P- and S-waves are windowed by the same length; and (2) rms amplitudes are computed by

$$A_{rms} = \sqrt{\frac{1}{T}\int_{t_o}^{t_o+T} [A(t)]^2 dt},$$

where $t_o$ is P- or S-wave and corresponding tube wave arrival time and $T$ is the window length; then (3) each tube wave rms amplitude is normalized by the corresponding P- or S-wave rms amplitude and the ratio is obtained by division. In the average spectral ratio method, the ratios of the S-wave generated tube wave to the P-wave generated

tube wave are obtained by dividing the respective spectra after the normalization of the corresponding P- or S-wave spectra over the usable bandwidth (80 to 200 Hz), and then by averaging. The normalized ratios of the S-wave generated tube wave to the P-wave generated tube wave are estimated for primary tube waves from the fractures at the depths of 232, 287, and 513 m, and presented in Table 2. Two independent estimations show reasonable agreement.

## Results

The two independent estimations of normalized ratios of S-wave generated tube to P-wave generated tube waves are inverted separately for the orientation of the three major fractures. In the inversion, the P- and S-wave velocities from the full-waveform acoustic logging are used for the formation velocities. Those are 6.8 and 3.8 km/s at the depth of 232 m, and 5.9 and 3.4 km/s at the depths of 287 and 513 m. Densities are assumed to be 2.8 at 232 m, and 2.7 at 287 and 513 m. Straight rays from the sources to the fracture intersections at the borehole are assumed. The inversion results are presented in Table 3. The results are affected by the survey geometry which is not optimal for this type of analysis. The offset of S/P#1 is much smaller than the other two shot points and its azimuth is almost opposite to S/P#3. The inversion results are more sensitive to S/P#1 than the others. These effects of survey geometry were discussed in detail previously. In spite of this, the inversion results for each fracture using different independent normalized tube wave ratio estimations are very similar. The largest discrepancy shown for the fractures at the depth of 232 m does not exceed $10^o$ in both the dip direction and angle. This confirms the stability of the inversion scheme in the presence of noise, which was shown previously by the numerical tests. Furthermore, in comparison with measurements from borehole televiewer images, there is reasonable agreement, except for the fracture at 232 m. The differences for the fractures at 287 and 513 m are about $10^o$ in the dip direction and about $20^o$ in the dip angle. If the measurement errors of the dip direction and angle in the televiewer images are considered, the agreement appears to be more reasonable.

The discrepancy between the inversion results and the measurements from televiewer images may be attributed to:

1. The bending ray due to inhomogeneities; if the media are only vertically inhomogeneous, the effects corrupt the dip angle estimations. The geology at the Kent Cliffs site shows lateral inhomogeneity. In this case, the seismic rays deviate from the sagittal plane, and the dip direction estimations are corrupted too.

2. Possible SH-wave motion caused by anisotropy or lateral inhomogeneity; since the vertical impact sources are used, only P- and SV-waves are expected. Also the borehole is in theory completely transparent to the incident SH-wave for low frequency approximation (Schoenberg, 1986), so that SH-type motion was excluded in the modeling and the inversion. The SH-wave particle motion, however, can cause the fracture wall motion in the normal direction. Significant seismic

anisotropy caused by rock and crack fabrics has been reported at the Kent Cliffs site by Lee (1990).

3. The variation of the fracture orientation away from the well. Those measured from televiewer image represent the fractures as they intersect the borehole. On the other hand, the results from this method represent the average over the fracture planes for much larger radii (generally on the order of a meter, although the effective fracture radius depends on the frequency content, the fracture permeability, fluid viscosity, and fluid compressibility).

Toksöz *et al.* (1992) found very shallow dipping angle (7°) with a 191° dip direction for the fracture at the depth of 232 m from inversion of tube waves generated by P-waves. Although they used the same data used in this study, the analysis was carried out independently with a different inversion algorithm. The qualitative agreement of these two independent studies for the fracture at the depth of 232 m suggests that the fracture in large scale is much less steep then the one measured from the televiewer image. This inference is also supported by the normalized amplitude ratios of S-wave generated tube waves to P-wave generated tube waves computed by the forward modeling equation. The ratios for the fracture orientations estimated from the borehole televiewer images (Table 1) and inversions (Table 3) are listed in Table 4. Table 4 shows that a large value of the normalized amplitude ratio for S/P#1 and a small value of it for S/P#2 for the fracture at the depth of 232 m would be required to have as steep dip angle as estimated from the televiewer images. However, both of the rms amplitude and average spectral ratio methods shows the opposite values (small for S/P#1 and large for S/P#2), which is in fact the case as observed in the data (Figures 11–14. It is worthwhile to note that the fractures at the depths of 287 and 513 m show an orientation trend similar to that of the formation fabric (foliation). It is suggested that adding a new source to existing VSP data sets at the Kent Cliffs test well will significantly improve the reliability of the results of the present study and provide a more adequate test of the theory presented here.

## DISCUSSION

A new technique to determine the orientation of open fractures using the normalized ratios of a S-wave generated tube wave to a P-wave generated tube wave is developed. These ratios can be estimated easily in hydrophone VSP or cross-well seismic profile sections. Numerical examples show that a set of two independent measurements of these ratios with polarization information, or a set of three independent measurements without polarization information, provides a unique solution. In order to get good results, it requires waves with similar inclinations and well distributed azimuths, and this can be achieved by the experiment design-arrangement of the source locations. The developed technique is stable in the presence of noise. Numerical tests show that only a two degree error in the dip direction and angle is found when inverting a set of three

ten percent-noisy data from a well-arranged experiment.

The new technique is applied to the hydrophone VSP data from the Kent Cliffs test well in southeastern New York state. The amplitude ratios of the primary S-wave-generated tube wave to the P-wave-generated tube wave are inverted to obtain the orientations of the major fractures at depths of 232, 287, 513 m. Although the hydrophone VSP experiment was not adequately designed to use this technique, good results were obtained. In comparison with other independent observations, such as borehole televiewer images, the results agree reasonably with others. The discrepancy may be attributed to the effects (which were not taken in account in the present study) of the deviation of rays from the straight lines due to inhomogeneity and the possible SH-type motion due to inhomogeneity and/or anisotropy. Alternatively the discrepancy may be attributed to the fact that the borehole televiewer samples only a small area of each fracture at the borehole, whereas the tube waves sample the formation over a much larger area.

## ACKNOWLEDGMENTS

The authors wish to thank Dr. W. Rodi and Prof. D. Morgan for discussions and comments. We acknowledge M.I.T.'s Earth Resources Laboratory Founding Members for their fellowship support for J. M. Lee. The hydrophone VSP data collection was supported by the Empire State Electric Energy Research Corporation through a contract with Woodward-Clyde Consultants. The basic data processing was carried out by J. M. Lee as a part of his Ph.D. dissertation at the Pennsylvania State University under the supervision of Prof. S. Alexander.

## REFERENCES


Beydoun, W.B., C.H. Cheng, and M.N. Toksöz, Detection of open fractures with vertical seismic profiling, *J. Geophys. Res., 90,* 4557–4566, 1985.

Hardin, E.L., and M.N. Toksöz, Detection and characterization of fractures from generation of tube waves, *Trans. SPWLA Ann. Logging Symp 26th,* II1–II21, 1985.

Hardin, E.L., C.H. Cheng, F.L. Paillet and J.D. Mendelson, Fracture characterization by means of attenuation and generation of tube waves at fractured crystalline rock at Mirror Lake, New Hampshire, *J. Geophys. Res., 92,* 7989–8006, 1987.

Huang, C.F. and J.A. Hunter, The correlation of "tube wave" events with open fractures in fluid-filled boreholes: current research, part A, *Geol. Surv. Canada Pap., 81-1A,* 361–376, 1981.

Huang, C.F. and J.A. Hunter, A seismic "tube wave" method for in-situ estimation of fracture permeability in boreholes, *Geophysics, 47,* 414, 1982.

Lee, J.M., In situ seismic anisotropy and its relationship to crack and rock fabrics, Ph.D. Thesis, The Pennsylvania State University, 1990.

Lee, J.M. and S.S. Alexander, An advanced F-K filter for VSP data, *EOS Trans. Amer. Geophys. Union, 70,* 15, 390, 1989.

Peng, C., J.M. Lee, and M.N. Toksöz, Pressure in a fluid-filled borehole due to a seismic source in stratified media, *submitted to Geophysics,* 1994.

Ratcliffe, N.M., The Ramapo fault system in New York and adjacent northern New Jersey: a case of tectonic heredity, *Geol. Soc. Am. Bull., 82,* 125–142, 1971.

Schoenberg, M., Fluid and solid motion in the neighborhood of fluid-filled borehole due to the passage of low-frequency elastic plane wave, *Geophysics, 51,* 1191–1205, 1986.

Statton, C.T., *Kent Cliffs Borehole Research Project: A determination of the magnitude and orientation of tectonic stress in southeastern New York state,* Woodward-Clyde Consultants Research Report EP 84–27, Wayne, New Jersey, 1986.

Toksöz, M.N., C.H. Cheng, and R.D. Cicerone, Fracture detection and characterization from hydrophone vertical seismic profiling data, in *Fault Mechanism and Transportation Properties of Rocks,* B. Evans and T. Wong, eds., Academic Press, London, 389–414, 1992.

Toksöz, M.N., Cicerone, R.D., J.M. Lee and S.S. Alexander, Fracture detection and characterization from hydrophone VSP data, *Soc. Explor. Geophys. 57th Ann. Meeting, Expanded Abstr. with Biographies,* 695–696, 1987.

White, J.E., Signals in a borehole due to plane waves in the solid, *J. Acoust. Soc. Am., 25,* 906–915, 1953.

Zoback, M.D., In situ stress measurements in the Kent Cliffs research well, in *Kent Cliffs Borehole Research Project: A determination of the magnitude and orientation of tectonic stress in southeastern New York state,* Woodward-Clyde Consultants Research Report EP 84–27, Wayne, New Jersey, 1986.

Table 1: The fracture orientations measured from borehole televiewer logging images. These fractures generate the primary tube waves in hydrophone VSP sections.

| Fracture depth | Dip direction | Dip angle |
|---|---|---|
| 232 | $180^o$ | $60^o$ |
| 287 | $165^o$ | $60^o$ |
| 513 | $170^o$ | $75^0$ |

Table 2: The normalized amplitude ratios of S-wave generated tube waves to P-wave generated tube waves. Estimations are done by two independent methods—rms amplitude ratio and average spectral ratio.

| Fracture | S/P#1 | | S/P#2 | | S/P#3 | |
|---|---|---|---|---|---|---|
| depth(m) | rms amp. | ave. spec. | rms amp. | ave. spec. | rms amp. | ave. spec. |
| 232 | 0.38 | 0.34 | 1.38 | 1.14 | 3.48 | 2.50 |
| 287 | 1.12 | 1.02 | 1.37 | 1.30 | 0.88 | 1.42 |
| 513 | 2.15 | 1.98 | 0.77 | 0.97 | 1.51 | 1.39 |

Table 3: The fracture orientations obtained from inversion of normalized tube wave amplitude ratios in hydrophone VSP. Inversions are carried out separately using two independent estimations presented in Table 2.

| Fracture depth(m) | Rms amp. | | Ave. spec. | |
|---|---|---|---|---|
| | dip direction | dip angle | dip direction | dip angle |
| 232 | $151^o$ | $18^o$ | $161^o$ | $27^o$ |
| 287 | $177^o$ | $84^o$ | $177^o$ | $84^o$ |
| 513 | $177^o$ | $50^o$ | $177^o$ | $53^o$ |

Table 4: The computed normalized amplitude ratios of S-wave generated tube waves to P-wave generated tube waves. Computations are done for fracture orientations estimated from the borehole televiewer images and inversions using the forward modeling equation.

| Fracture depth(m) | BH TV | | | Rms amp. | | | Ave. spec. | | |
|---|---|---|---|---|---|---|---|---|---|
| | S/P#1 | S/P#2 | S/P#3 | S/P#1 | S/P#2 | S/P#3 | S/P#1 | S/P#2 | S/P#3 |
| 232 | 5.86 | 0.14 | 2.28 | 0.37 | 1.37 | 4.11 | 0.33 | 1.03 | 4.02 |
| 287 | 7.15 | 0.24 | 6.02 | 1.00 | 1.41 | 1.62 | 1.00 | 1.41 | 1.62 |
| 513 | 22.34 | 4.08 | 7.10 | 2.72 | 0.76 | 3.34 | 2.60 | 1.05 | 3.30 |

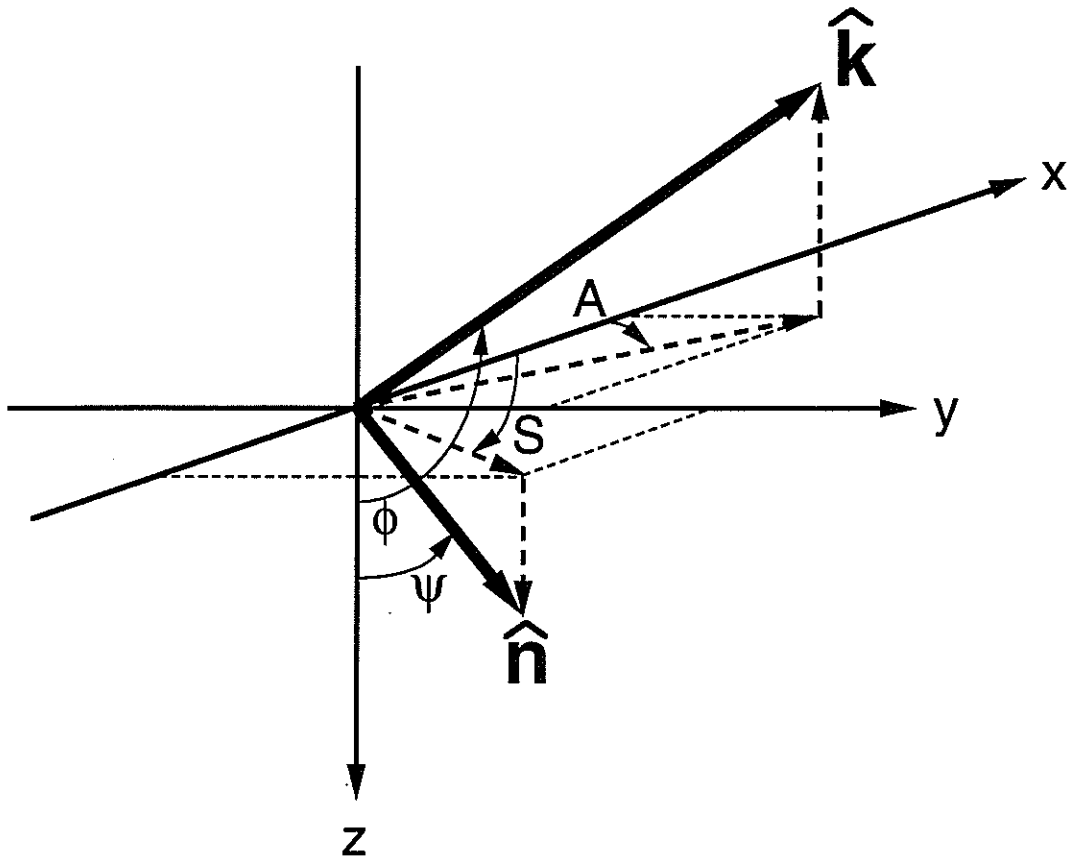


Figure 1: Geometry of the unit wave vector, $\hat{\mathbf{k}}$, and unit fracture normal vector, $\hat{\mathbf{n}}$; a right-handed system is chosen with $z$ increasing downward. Since the $x$-axis is considered as north, $S$ and $\psi$ are called the dip direction and dip angle of the fracture, and $A$ and $\phi$ are called the azimuth and inclination (measured from positive vertical) of the wave vector.

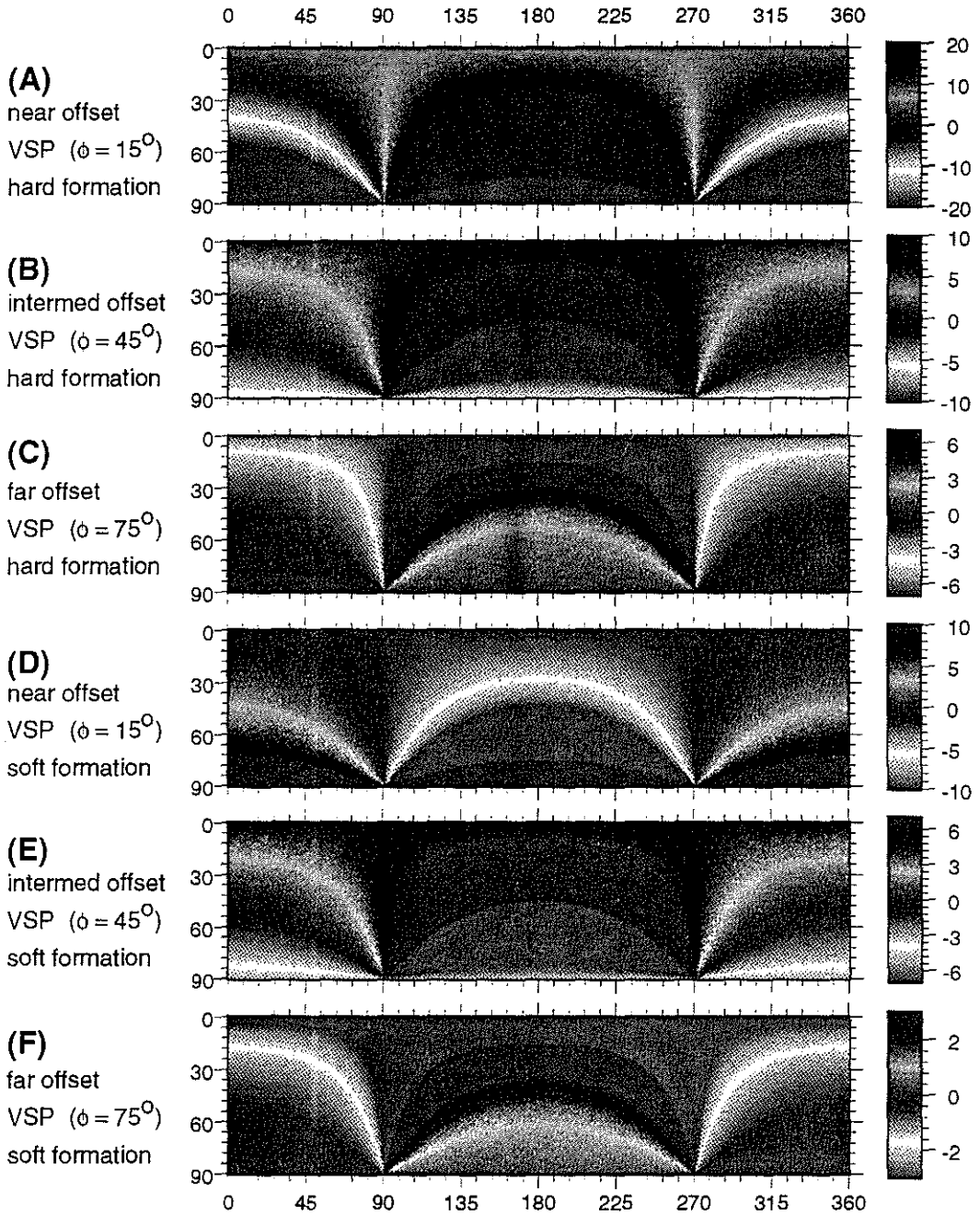


Figure 2: The ratio of tube wave amplitude generated by a plane SV-wave to that by a P-wave as function of the fracture dip direction and dip angle. The tube wave amplitudes are normalized by the amplitude of pressure inside the borehole caused by corresponding waves. A, B, and C are for a hard formation (Vp=5970 m/s, Vs=2880 m/s, $\rho$=2656 kg/m$^3$), and D, E, and F are for a soft formation (Vp=2074 m/s, Vs=869 m/s, $\rho$=2000 kg/m$^3$) with incident angles of 15$^o$, 45$^o$, and 75$^o$ respectively. The vertical axes represent the fracture dip angles and the horizontal axes represent the dip directions in degrees.

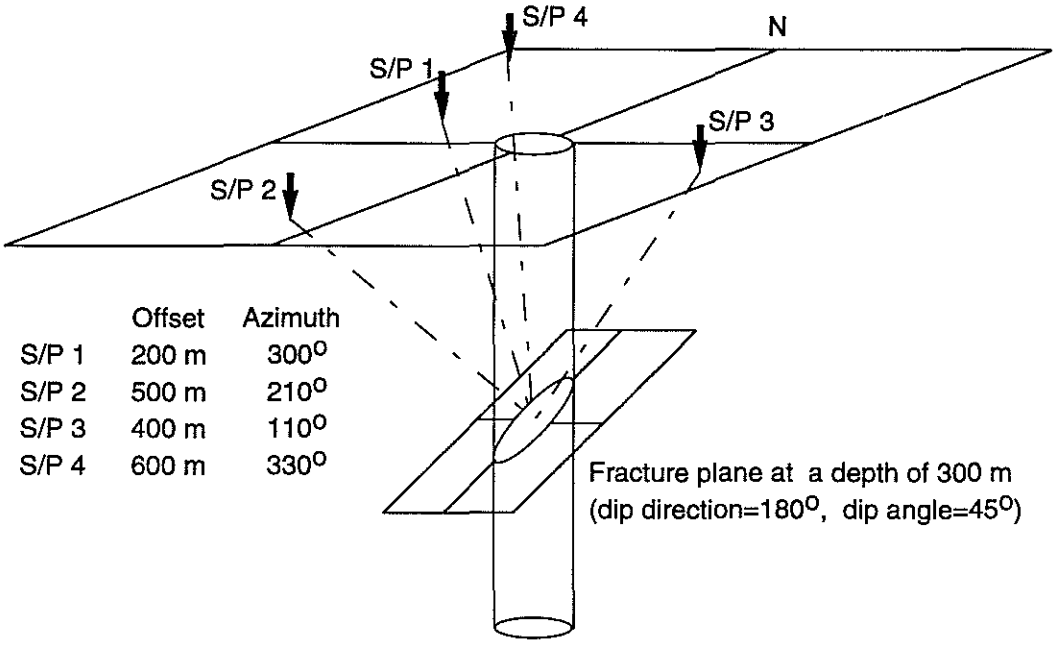


Figure 3: The schematic VSP geometry used to test the performance and stability of inversion. A fracture of 180° dip direction and 45° dip angle intersects the borehole at a depth of 300 m in a homogeneous hard formation of Vp=5970 m/s, Vs=2880 m/s, and $\rho$=2656 kg/m$^3$.

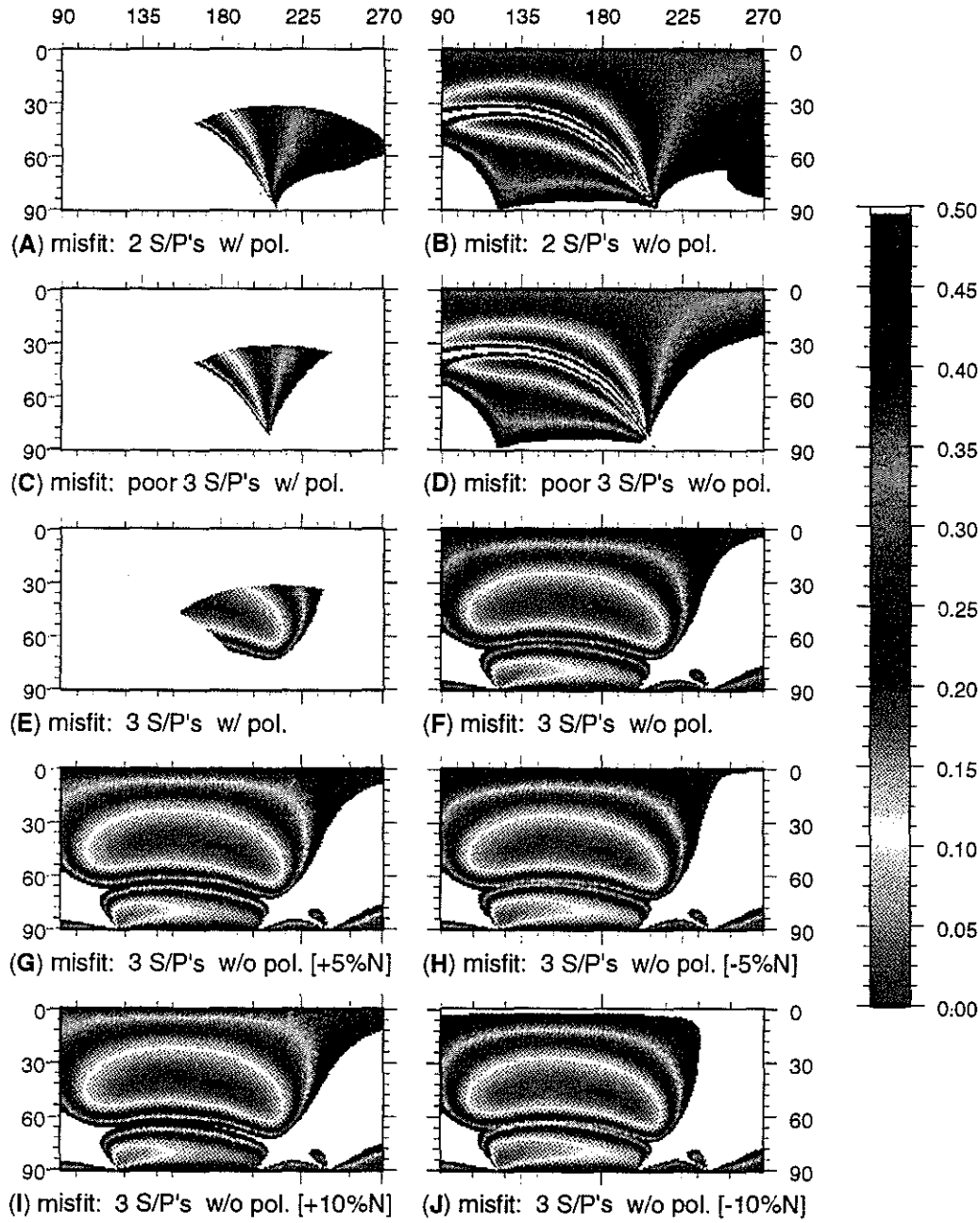


Figure 4: The misfit values as a function of the fracture orientation. For A and B, two shot points (S/P's 1 and 2), for C and D, three shot points (S/P's 1, 2, and 3), and for E to J, another three shot points (S/P's 2, 3, and 4) are used (see Figure 3 for geometry). The vertical axes represent the fracture dip angles and the horizontal axes represent the dip directions in degrees. Only misfit values for the range from $90^o$ to $270^o$ of the fracture dip direction are shown. Polarization information is used for A, C, and E. It is shown in F that tube wave amplitude ratios without polarization information from adequately chosen three shot points can provide a very reliable solution. The stability of the misfit function with respect to noise is shown in G to J.

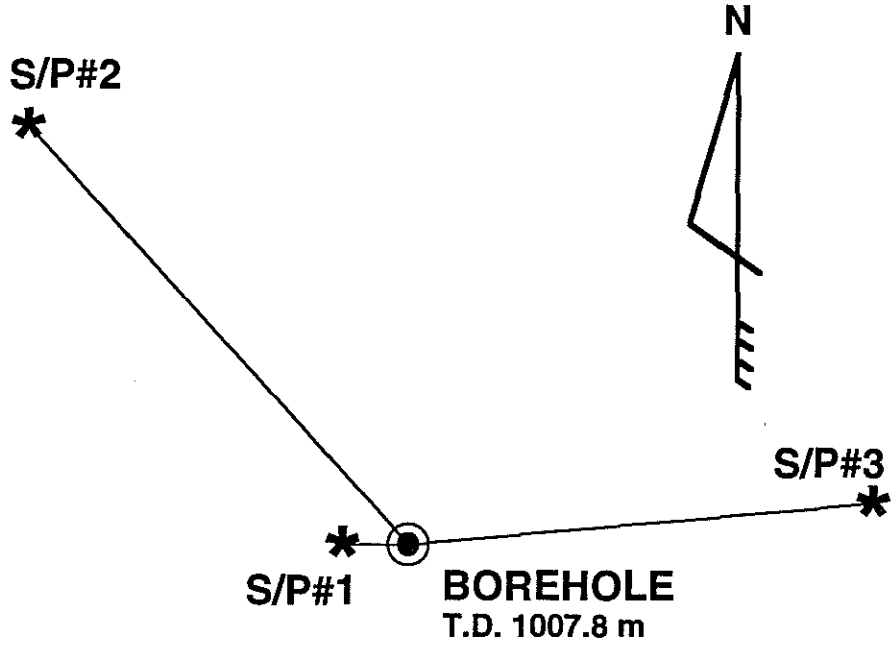


| | offset | azimuth | elevation* |
|---|---|---|---|
| S/P#1 | 37.5 m | 268° | 0.0 m |
| S/P#2 | 350.5 m | 318° | -3.4 m |
| S/P#3 | 288.0 m | 85° | -12.2 m |

*The elevation is relative to the well head.

Figure 5: Kent Cliffs hydrophone VSP shot point map; the source elevations relative to the well head are 0.0 m for S/P#1, −3.4 m for S/P#2, and -12.2 for S/P#3.

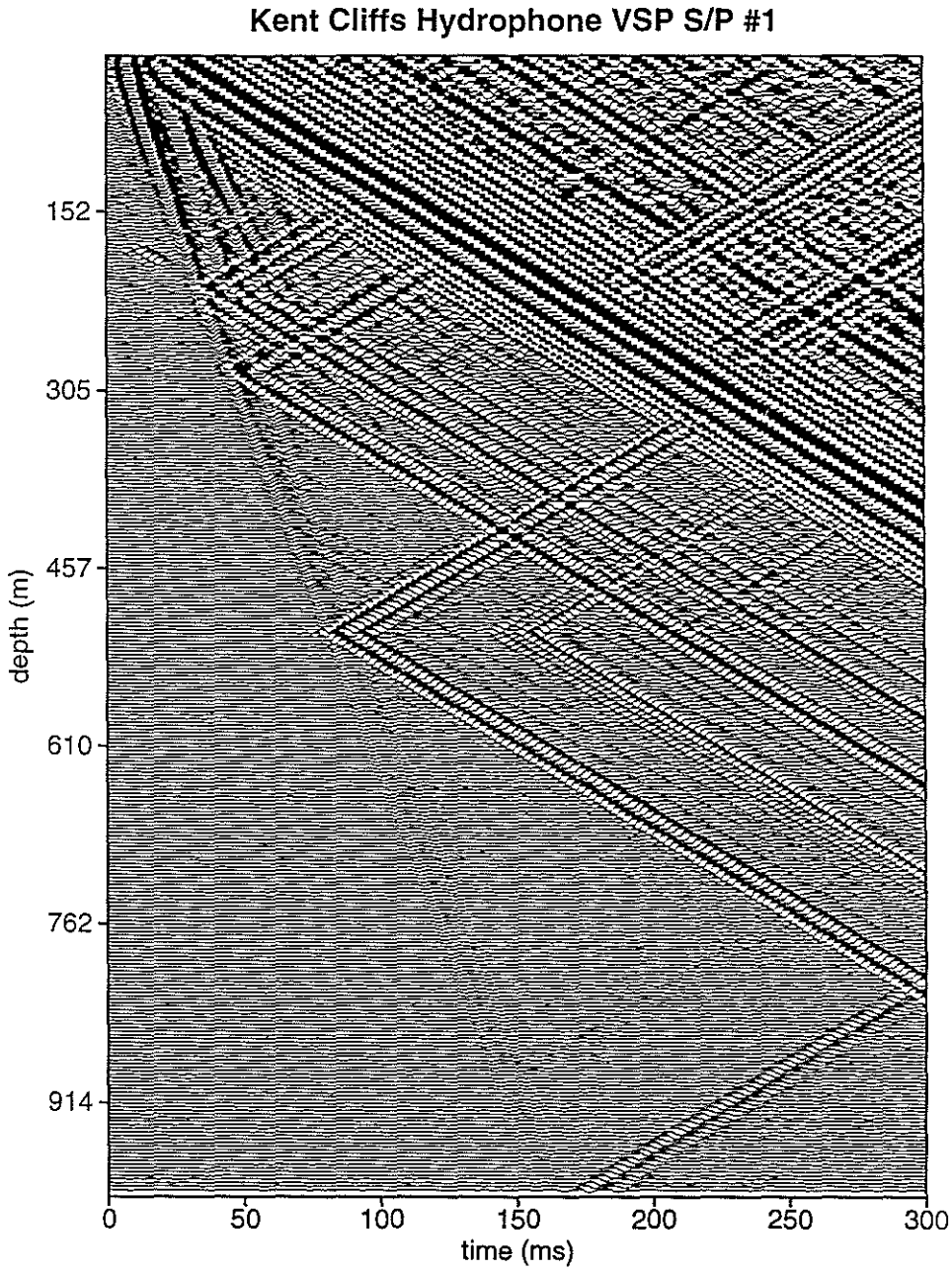


Figure 6: Hydrophone VSP section for S/P#1; The source offset is 37.5 m with an azimuth of S88°W. A band pass filter of a 80–200 Hz pass band is applied. The first hydrophone is at a depth of 21.34 m, slightly below the water table, and the last hydrophone is at a depth of 990.6 m, slightly above the well bottom.

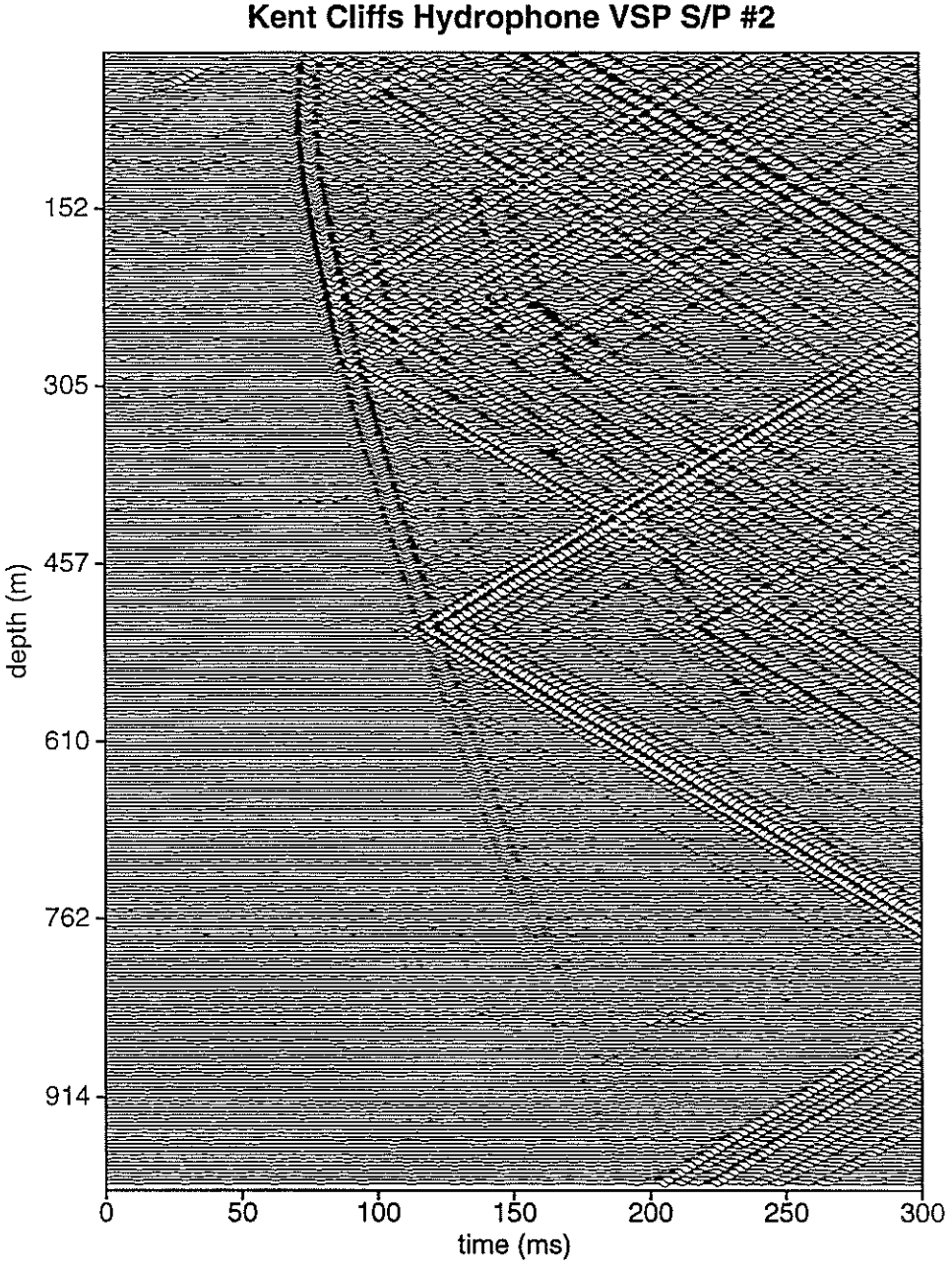


Figure 7: Hydrophone VSP section for S/P#2; the source offset is 350.5 m with an azimuth of N42°W. A band pass filter of a 80–200 Hz pass band is applied. The first hydrophone is at a depth of 21.34 m, slightly below the water table, and the last hydrophone is at a depth of 990.6 m, slightly above the well bottom.

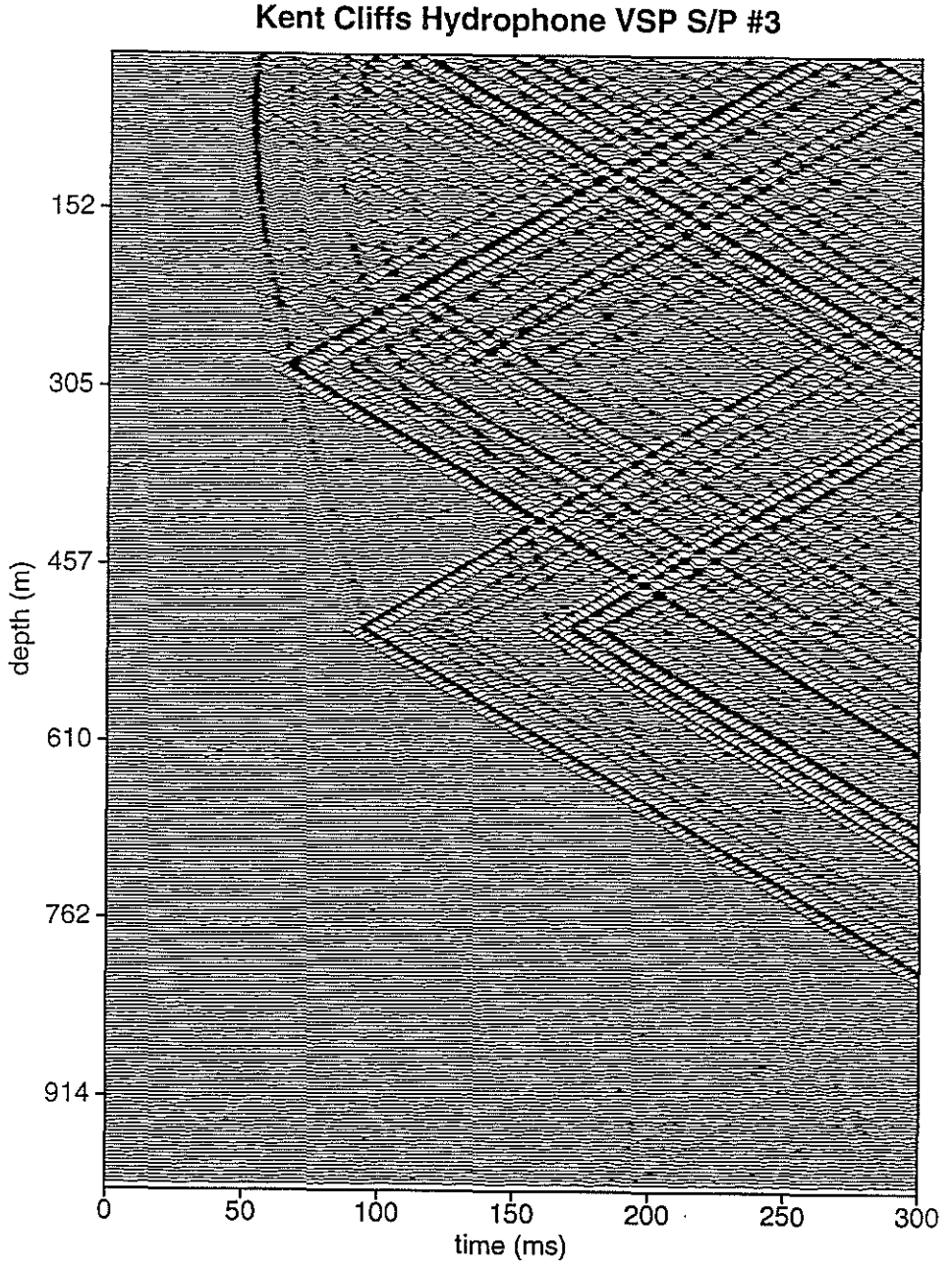


Figure 8: Hydrophone VSP section for S/P#3; the source offset is 288.0 m with an azimuth of N85°E. A band pass filter of a 80–200 Hz pass band is applied. The first hydrophone is at a depth of 21.34 m, slightly below the water table, and the last hydrophone is at a depth of 990.6 m, slightly above the well bottom.

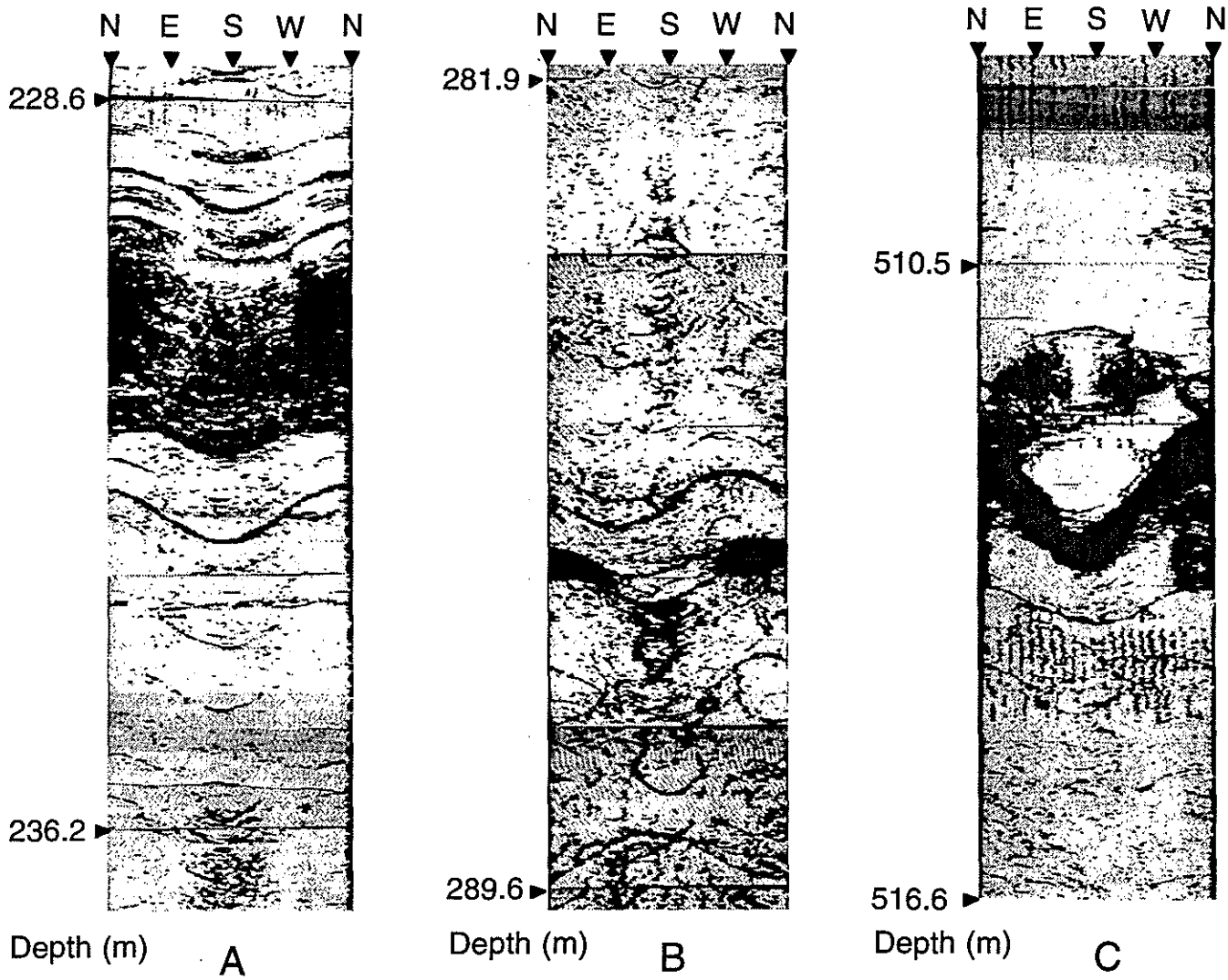


Figure 9: The borehole televiewer images at the depths around the fractures which generate primary tube waves in hydrophone VSP sections. (A) shows fractures whose dip direction is 180° and dip angle is 60° combined with shear zone at a depth of 232 m. (B) shows an open fracture whose dip direction is 165° and dip angle is 60° at a depth of 287 m. (C) shows an open fracture whose dip direction is 170° and dip angle is 75° at a depth of 513 m. It also shows that the part of the fracture which intersects the borehole by an acute angle has been chipped away.

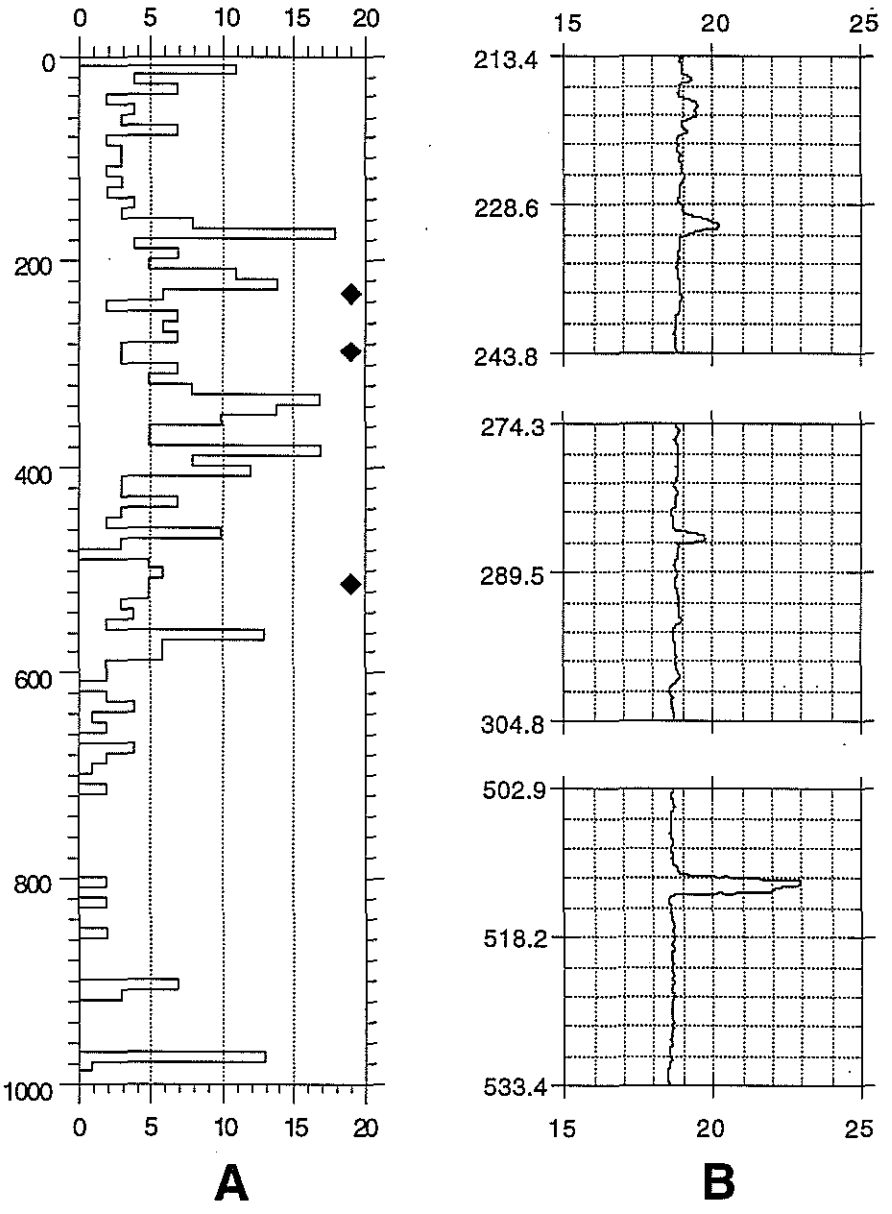


Figure 10: Fracture density obtained from the borehole televiewer logs and sections of the caliper logs. (A) Number of fractures per 10 m is presented as function of depth. Black diamonds indicate the locations of the major open fractures generating primary tube waves in hydrophone VSP. (B) Sections of the caliper logs show that the well diameter increase at the depths of these major open fractures. (redrawn from Zoback, 1986).

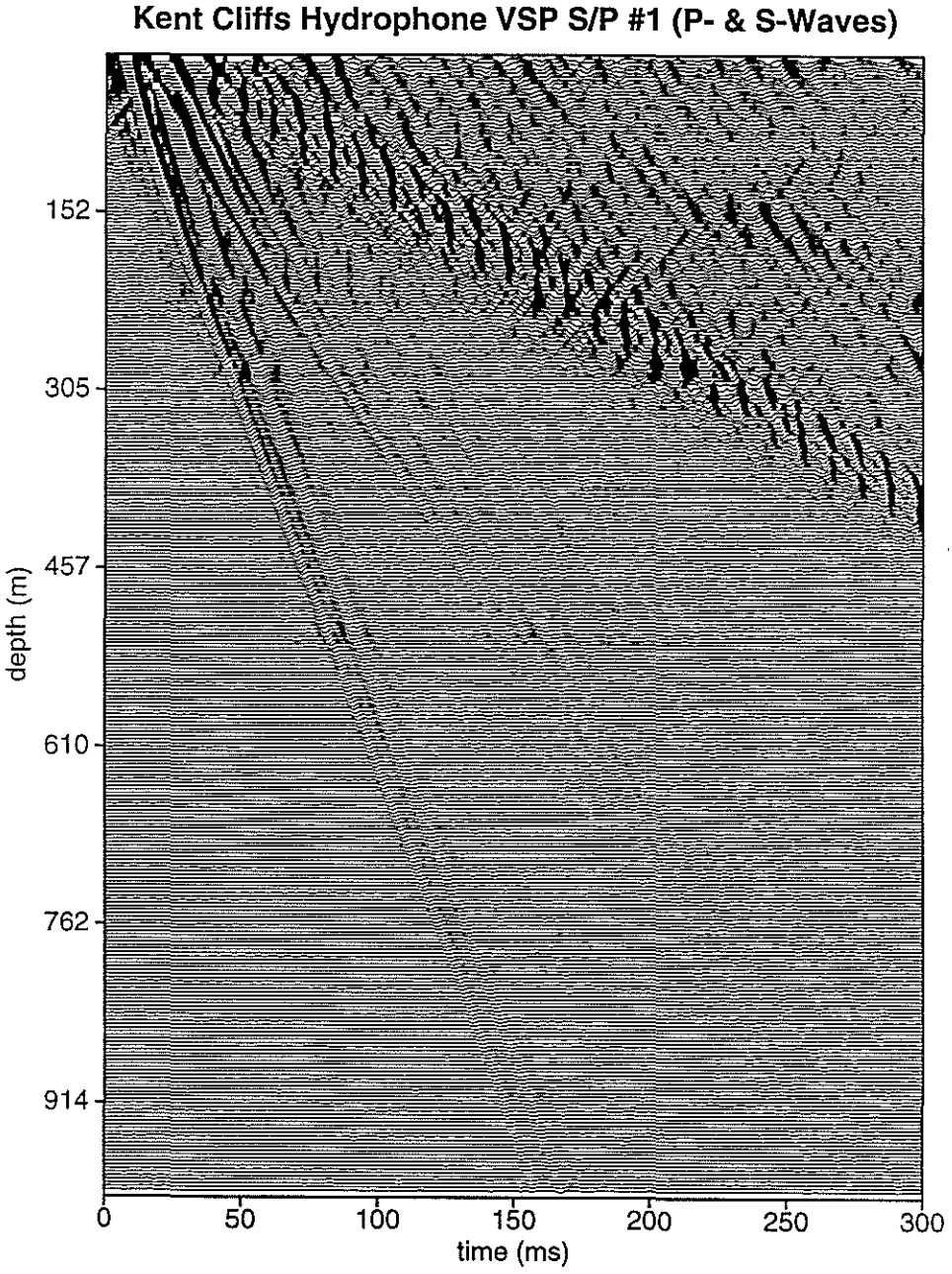


Figure 11: *f-k* filtered VSP section for S/P#1; P- and S-waves have been isolated. The remnant tube waves which start at the top of the borehole are caused by spatial aliasing.

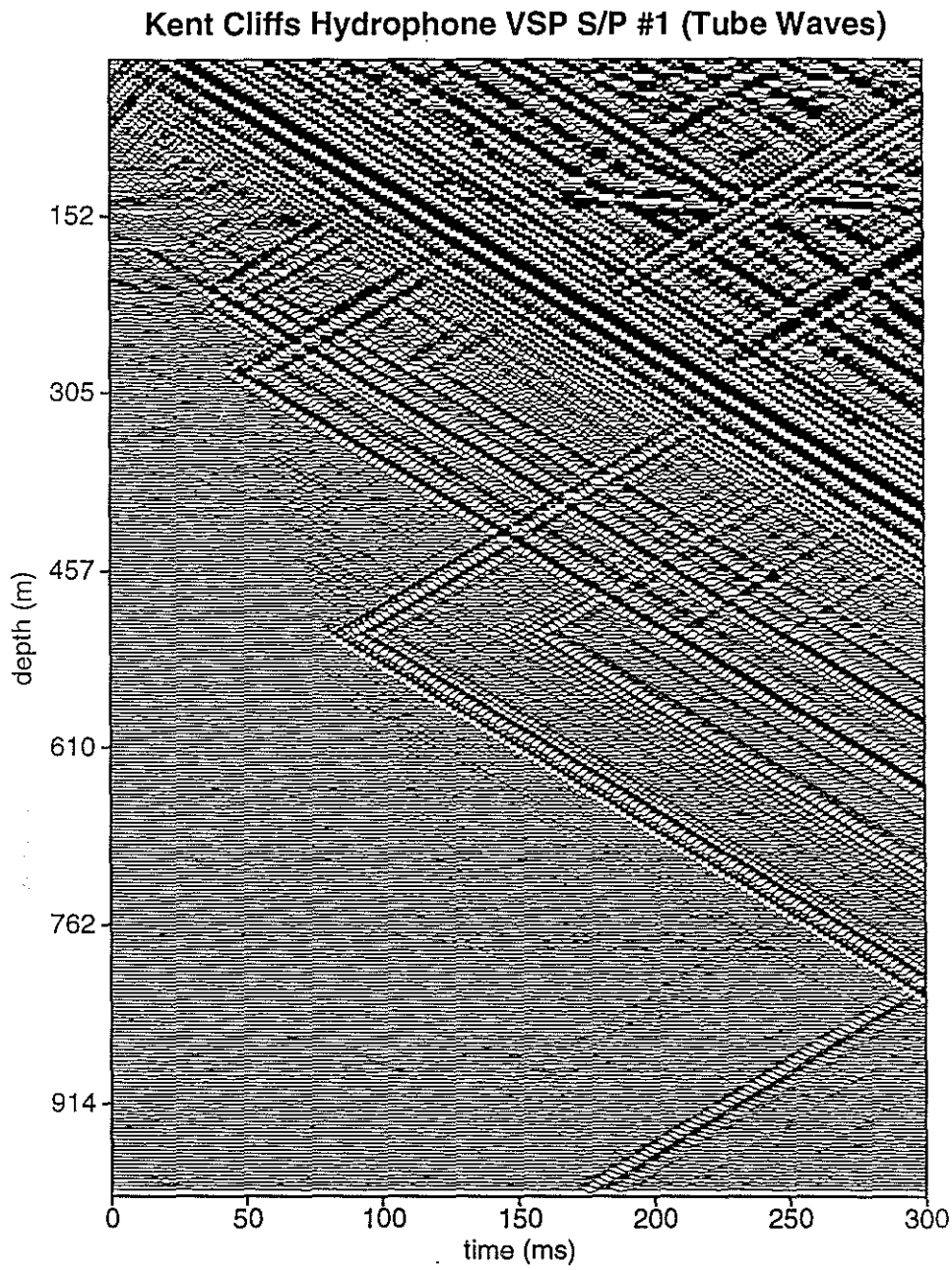


Figure 12: $f$-$k$ filtered VSP section for S/P#1. tube waves have been isolated.

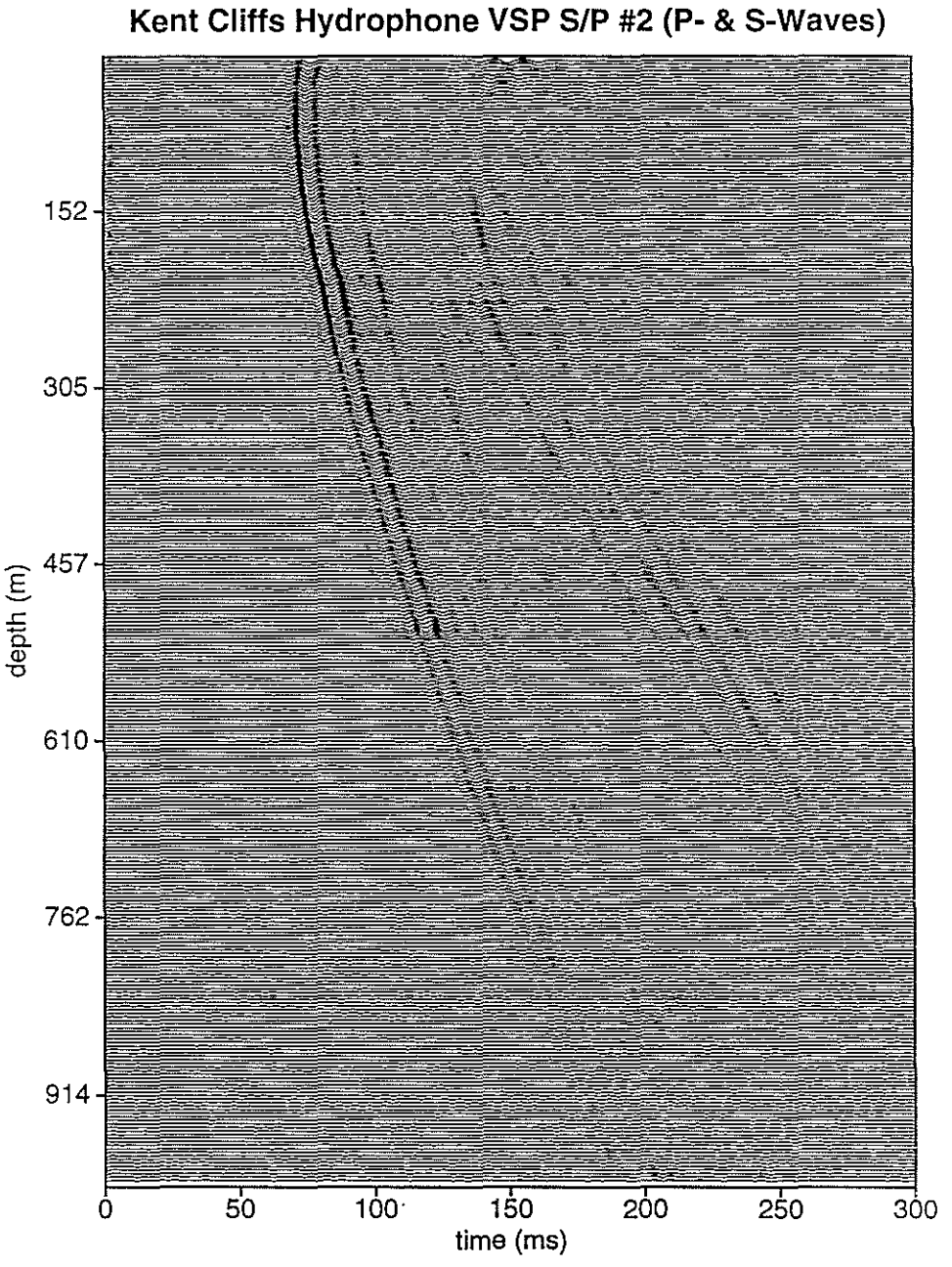


Figure 13: *f-k* filtered VSP section for S/P#2. P- and S-waves have been isolated.

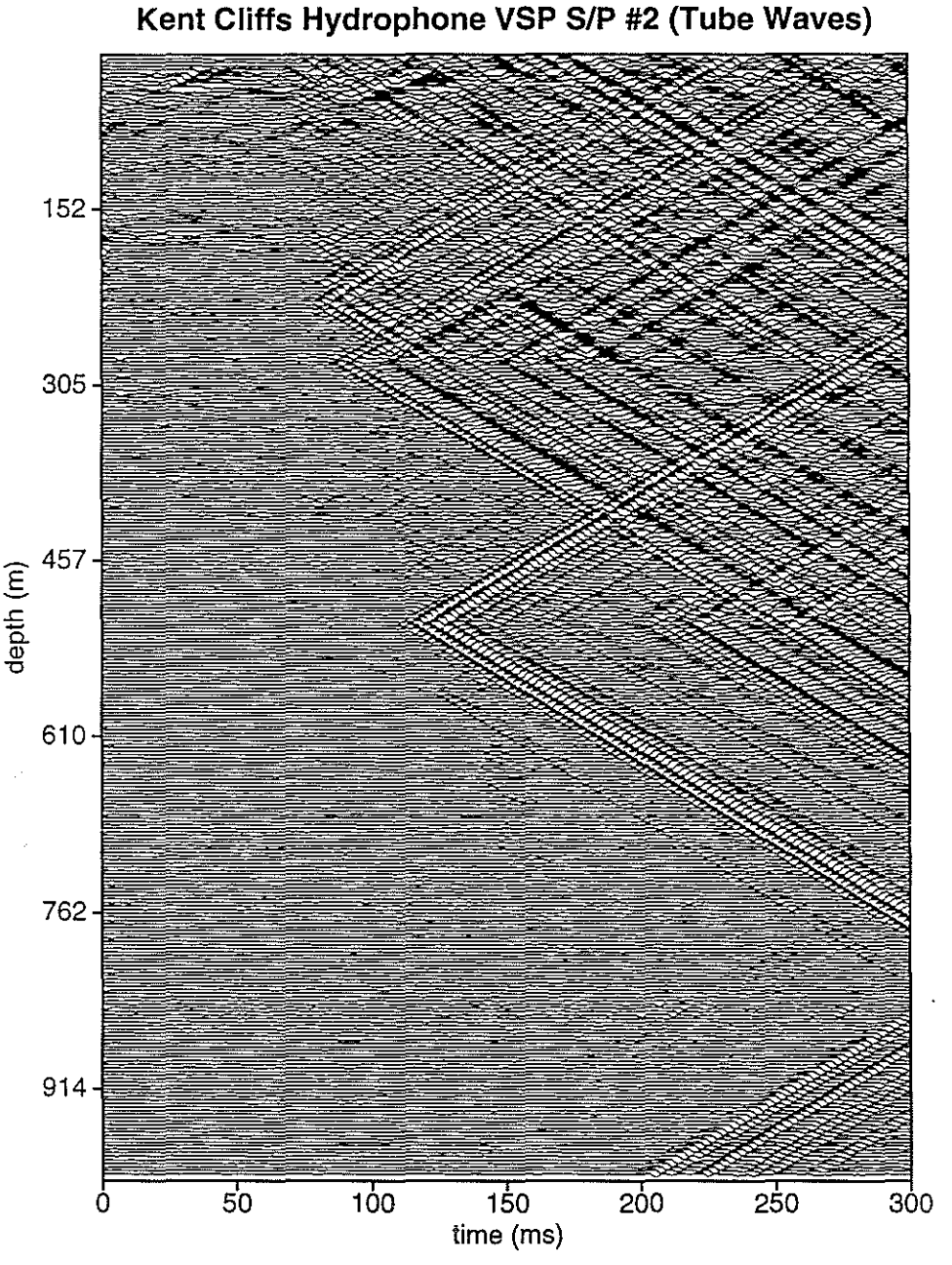


Figure 14: *f-k* filtered VSP section for S/P#2; tube waves have been isolated.

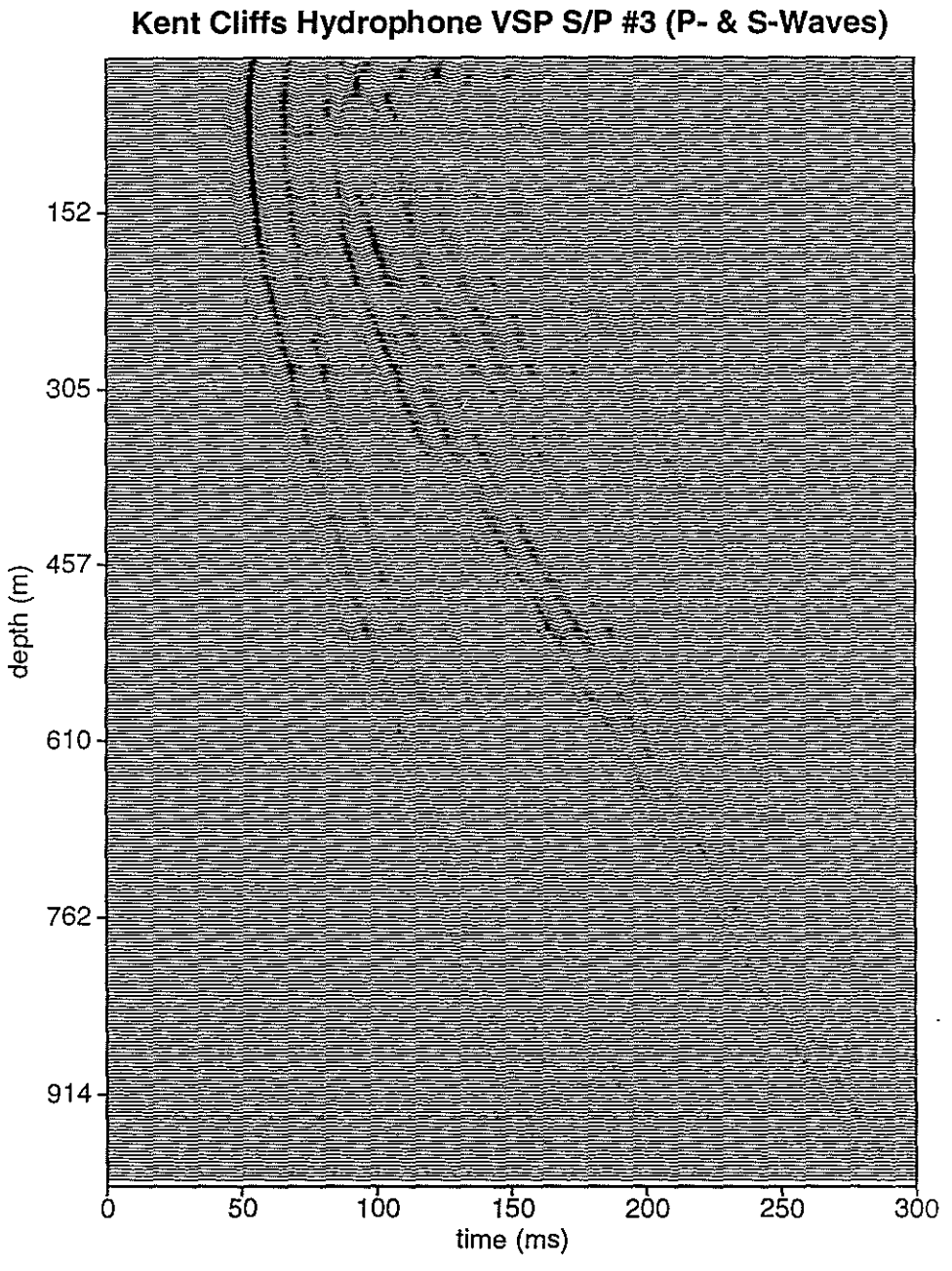


Figure 15: $f$-$k$ filtered VSP section for S/P#3; P- and S-waves have been isolated.

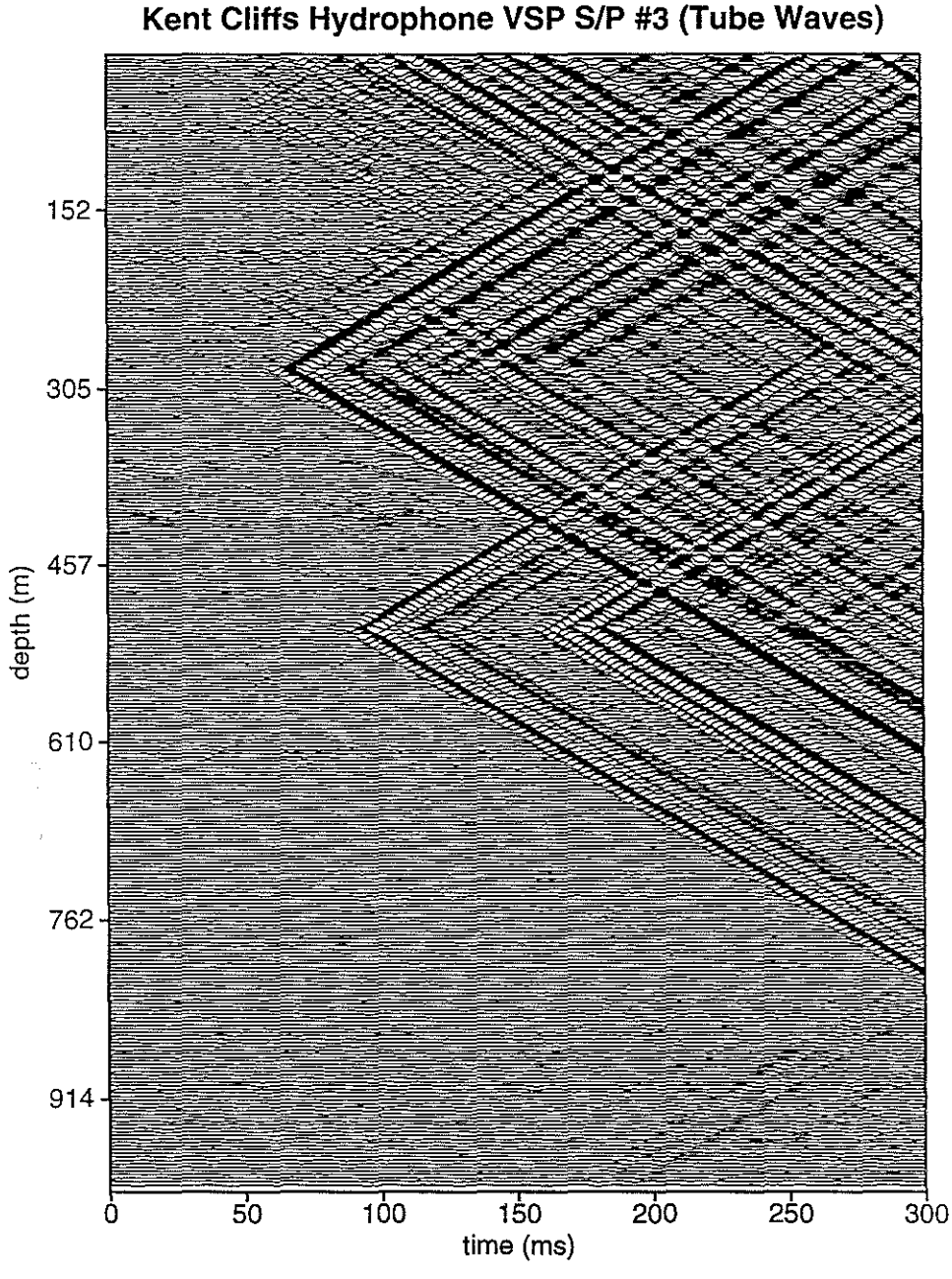


Figure 16: *f-k* filtered VSP section for S/P#3; tube waves have been isolated.